A general strategy to generate oxygen vacancies in bimetallic layered double hydroxide for water oxidation

Konglin Wu,*[a, b] Luoxiang Shi,[a] Zhendong Wang,[a] Ye Zhu,[a] Xinyue Tong,[a] Wenxiang He,[c] Junwei Wang,[c] Lirong Zheng,[e] Yanshang Kang,[a] Weilong Shan,[a] Zhiguo Wang,[d] Aijian Huang*[d] and Binbin Jiang*[a, c]

[a]Engineering Research Center of Biofilm Water Purification and Utilization Technology of Ministry of Education, Anhui University of Technology, Maanshan 243032, China

[b] Anhui Laboratory of Molecule-Based Materials, College of Chemistry and Materials Science, Anhui Normal University, Wuhu 241002, China

[c]School of Chemistry and Chemical Engineering, Anqing Normal University, Anqing 246001, China

[d] School of Electronics Science and Engineering, University of Electronic Science and Technology of China, Chengdu 610054, China

[e] Beijing Synchrotron Radiation Facility (NSRF), Institute of High Energy Physics, Chinese Academy of Science, Beijing 100049, China

Corresponding Authors:

*E-mail: klwuchem@ahut.edu.cn; (K. Wu); 201811022517@std.uestc.edu.cn (A. Huang); bbjiang0726@126.com (B. Jiang).

Materials

The $NiCl_2 \cdot 6H_2O$, $FeCl_3 \cdot 6H_2O$, $CoCl_2 \cdot 6H_2O$, urea and hexamethylenetetramine were supported by Sinopharm Chemical Reagent Co., Ltd. The Nafion (5 wt %) was obtained from Sigma-Aldrich Co. The commercial RuO_2 catalysts were supported by Alfa Aesar Co. Other reagents were analytical reagent grade without further purification. The distilled water was used throughout the experiments (Resistivity > 18.2 MΩ·cm).

The synthesis of CN/C

The CN/C was achieved based on followed procedures, in brief, 100 mg carbon black was dispersed in 100 mL doubly distilled water by ultrasound 4 h to form a homogeneous dispersion. Then 50 mg, 100 mg or 200 mg dicyandiamide was added into the above dispersion under continue stirring. After stirring with 12 h, the achieved composite was obtained by centrifugation and then dried with a freeze drying method. At last, the above mixture was annealed under Ar atmosphere at 550 °C for 1 h at a heating rate of 5 °C·min^{-1}. The achieved product was named as CN/C-1, CN/C and CN/C-2.

The synthesis of O_{v2}-NiFe hydroxide

O_{v2}-NiFe hydroxide was achieved via the followed procedures. Firstly, the 5 mg CN/C was dispersed into ethylene glycol with ultrasonication. Then, the 10 mL mixed solution (the molar of $NiCl_2 \cdot 6H_2O$ and $FeCl_3 \cdot 6H_2O$ is 0.2 mmol and 0.06 mmol, respectively) was added into the above solution under stirring. Subsequently, 140 mg $CO(NH_2)_2$ was put into the above solution with continuously stirring for 10 h. The last, the obtained homogeneous solution was added into the 25 mL Teflon-lined autoclave and heated at 120 °C for 10 h. The achieved product was washed with distilled water and dried in the vacuum oven. The O_{v1}-NiFe hydroxide, O_{v3}-NiFe hydroxide and NiFe hydroxide was synthesized according to the similar strategy by using CN/C-1, CN/C-2 and carbon black, respectively.

The synthesis of O_v-CoFe LDH hydroxide and O_v-CoNi LDH hydroxide

The as-prepared O_v-CoFe hydroxide was achieved through the simple hydrothermal approach. Firstly, the 10 mg CN/C was dispersed into deionized water with

ultrasonication. Then, the 10 mL mixed solution with 0.32 mM Co^{2+} and 0.16 mM Fe^{3+} was dropped into the above suspension under stirring. Subsequently, 10 mL mixed solution containing 76 mg NaOH and 38 mg Na_2CO_3 was added into the mixed solution with vigorous stirring. The achieved slurry was then transferred into a Teflon-lined stainless steel autoclave and heated at 80 °C for 48 h. The obtained product was washed with distilled water and dried in the vacuum oven. The CoFe hydroxide was synthesized according to the similar strategy.

The synthesis of O_v-CoNi hydroxide and CoNi hydroxide

The as-prepared O_v-CoNi hydroxide was achieved via the followed procedures. Firstly, the 5 mg CN/C was dispersed into deionized water with ultrasonication. Then, the 10 mL mixed solution (the molar ratio of Co, Ni is 2 : 1, and the total concertation of metal is 0.3 mM) was added into the above solution under stirring. Subsequently, 600 mg hexamethylenetetramine was put into the mixed solution with continuously stirring for 10 min. The last, the obtained homogeneous solution transferred into the 25 mL Teflon-lined stainless-steel autoclave and heated at 95 °C for 5 h. The achieved product was washed with distilled water and dried in the vacuum oven. The CoNi hydroxide was synthesized according to the similar strategy.

Materials characterizations

The as-prepared composites were characterized by XRD (Philips X'pert PRO MPD diffractometer, λ_{Cu} = 0.15406 nm), scanning electron microscopy (SEM, Zeiss Supra 55), transmission electron microscope (TEM), high resolution (HRTEM), high angle annular dark field scanning transmission electron microscopy (HAADF-STEM) and elemental mapping by energy-dispersive X-ray spectrometry (EDS) with FEI Tecnai F20 transmission electron microscope (accelerating voltage of 200 kV), respectively. The chemical states and electronic structure of composites were performed by using the X-ray photoelectron spectroscopy (XPS) on a Kratos AXIS UltraDLD ultrahigh vacuum surface analysis system with Al Kα radiation (1486 eV) as a probe. Metal content of obtained composite was determined by ICP-OES (Agilent 720). The Fourier transform infrared (FTIR) spectra of the composite were recorded from the Hyperion spectrophotometer (Bruker) at the scan range of 4000 – 400 cm^{-1}.

Electrochemical Measurement

All electrochemical measurements were tested by CHI 760 E electrochemical workstation via the three-electrode systems. Where the carbon rod, Ag/AgCl electrode and modified glass carbon electrode (GCE, 3 mm) was employed as the counter electrode, reference electrode, and working electrode, respectively. For the preparation of the working electrode, the 4 mg composites were dispersed in mixed solution (100 µL Nafion solution (0.5 wt%), 750 µL distilled water and 150 µL isopropanol) by sonication to form the homogeneous ink. Then the 6 µL link was loaded onto the GCE and dried at the room temperature. The composite were uniformly loaded onto a GCE with a total loading of 509 $\mu g \cdot cm^{-2}$. In this work, all electrochemical data was calculated vs. the reversible hydrogen electrode (RHE) according to the following the equation. E (RHE) = E (Ag/AgCl) + 0.059 × pH + 0.197V. The overpotential (η) was calculated by η (V) = E (RHE) − 1.23 V. Before the OER test, the CV was conducted from the 1.0 to 1.6 V vs. RHE at a scan rate of 5 $mV \cdot s^{-1}$ until the reproducible voltammograms were achieved. The stability of composite was recorded by chronopotentiometry at 10 $mA \cdot cm^{-2}$. The double-layer capacitance (C_{dl}) was estimated by CV at a potential range from 1.10 to 1.30 V vs. RHE. The electrochemical impedance spectroscopy was acquired in a frequency range from 0.1 Hz to 100 kHz.

DFT computational methods. All of the calculations were performed by means of spin polarized density functional theory (DFT) methods using the Vienna Ab initio Simulation Package (VASP) [S1]. While the projector augmented wave (PAW) method was adopted to describe electron-ion interaction [S2]. The Perdew-Burke-Ernzerhof (PBE) exchange-correlation functional within a generalized gradient approximation (GGA) was employed, and a 450 eV cut off energy for the plane-wave basis set was used for the valence electrons. The self-consistent filed (SCF) calculations were performed with an energy and force convergence criterion of 10^{-5} eV and 0.02 eV $Å^{-1}$, respectively. GGA+U is adopted for Ni-3d and Fe-3d orbitals owing to the failure of DFT to describe strong correlation of d orbital of transition metal [S3]. The Hubbard U value was set 5.20 eV for Ni and 2.56 eV for Fe [S4, S5].

A DFT-D3 scheme [S6] of dispersion correction was used to describe the van der Waals (vdW) interactions in molecule adsorption. And the intrinsic dipole correction was also considered in all DFT calculations. The Brillouin zone was sampled using the 4×4×1 Monkhorst-Pack sampling in structure optimization for periodically repeated slabs with maximum symmetry applied to reduce the number of k-points in the calculations. To avoid the interactions between two adjacent periodic images, the vacuum thickness was set to be 15 Å. The atomic structures were analyzed by using the VESTA code [S7].
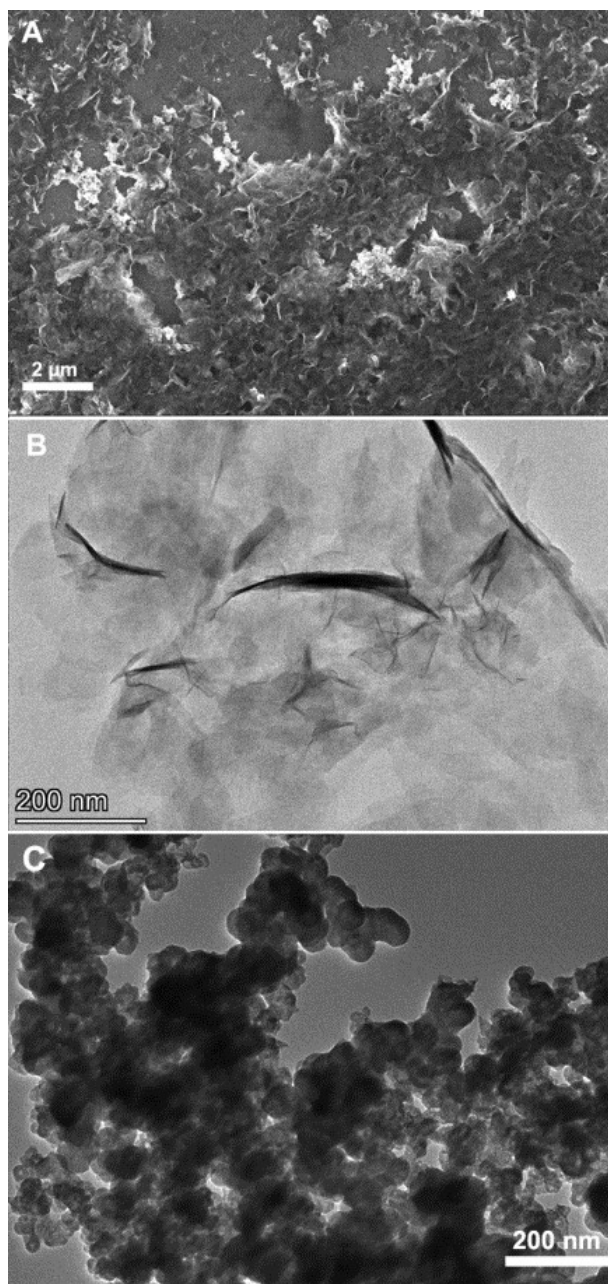
Fig. S1. The (**A**) SEM, (**B**) TEM image of NiFe hydroxide and (**C**) SEM image of CN/C.
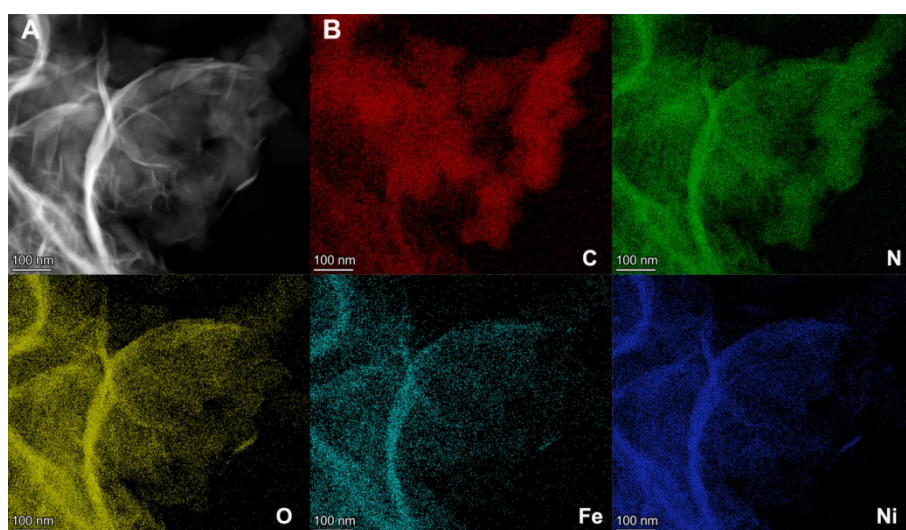
Fig. S2. (**A**) High angle annular dark field scanning transmission electron microscopy (HAADF-STEM) image and (**B**) corresponding energy-dispersive X-ray spectrometry (EDX) mapping of O_{v2}-NiFe hydroxide.
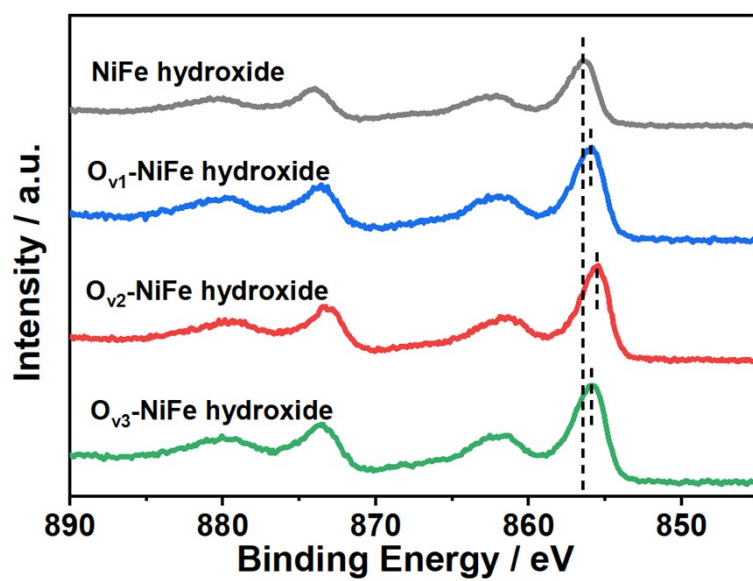
Fig. S3. Ni 2p spectra of NiFe hydroxide, O_{v1}-NiFe hydroxide, O_{v2}-NiFe hydroxide and O_{v3}-NiFe hydroxide
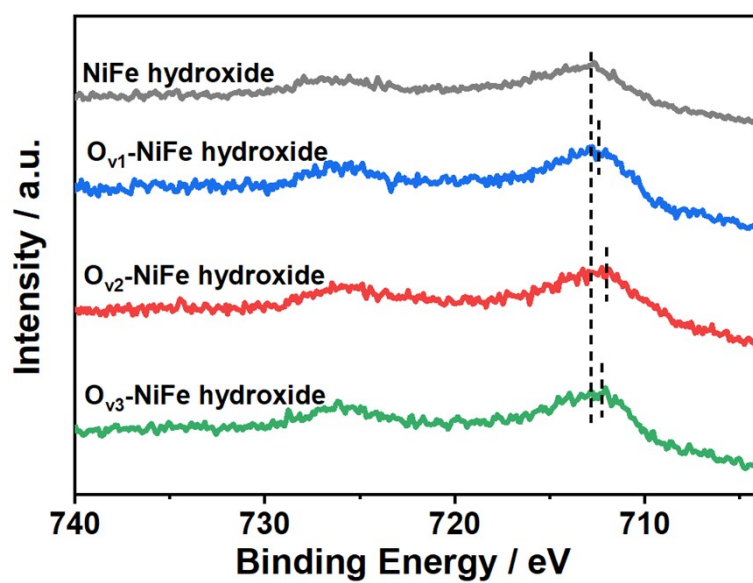
Fig. S4. Fe 2p spectra of NiFe hydroxide, O_{v1}-NiFe hydroxide, O_{v2}-NiFe hydroxide and O_{v3}-NiFe hydroxide
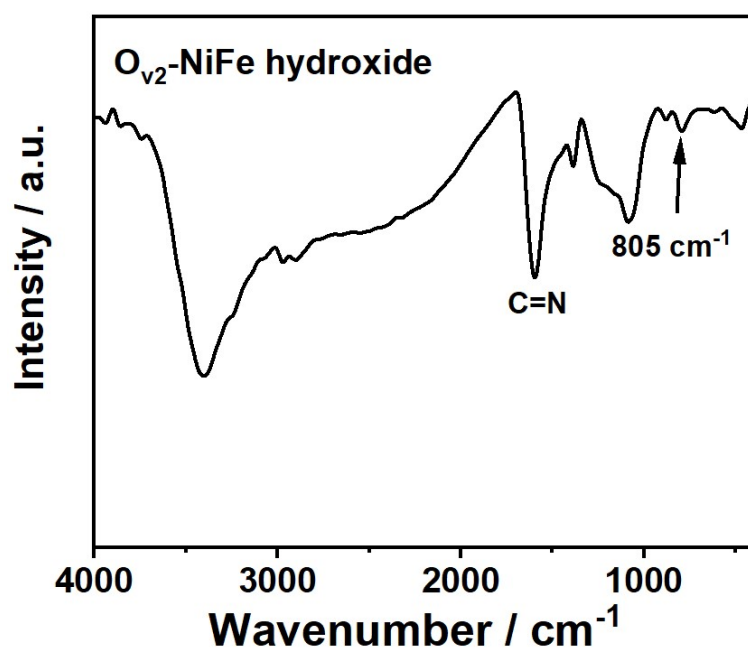
Fig. S5. The FTIR spectrum of O_{v2}-NiFe hydroxide.
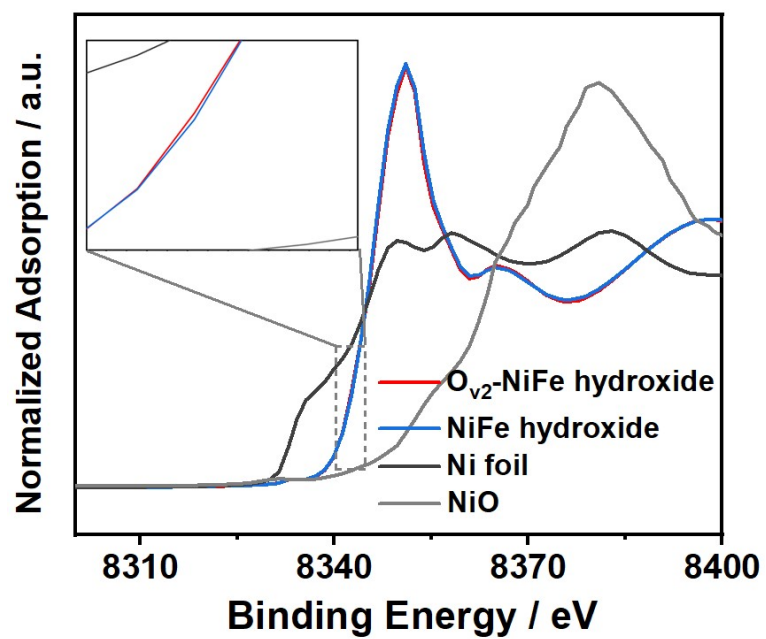
Fig. S6. Ni K-edge XANES spectra of Ni foil, NiO, NiFe hydroxide and O_{v2}-NiFe layered double hydroxide.
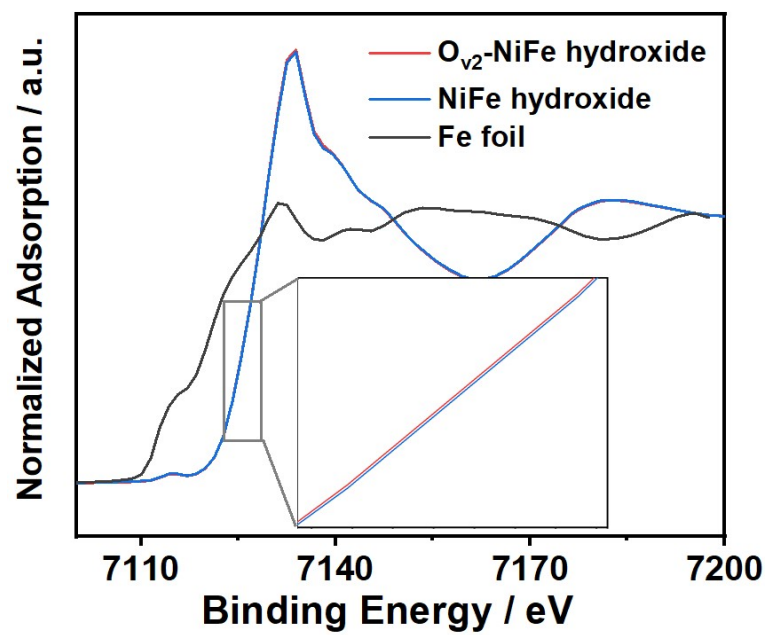
Fig. S7. Fe K-edge XANES spectra of Ni foil, NiO, NiFe hydroxide and O_{v2}-NiFe hydroxide.
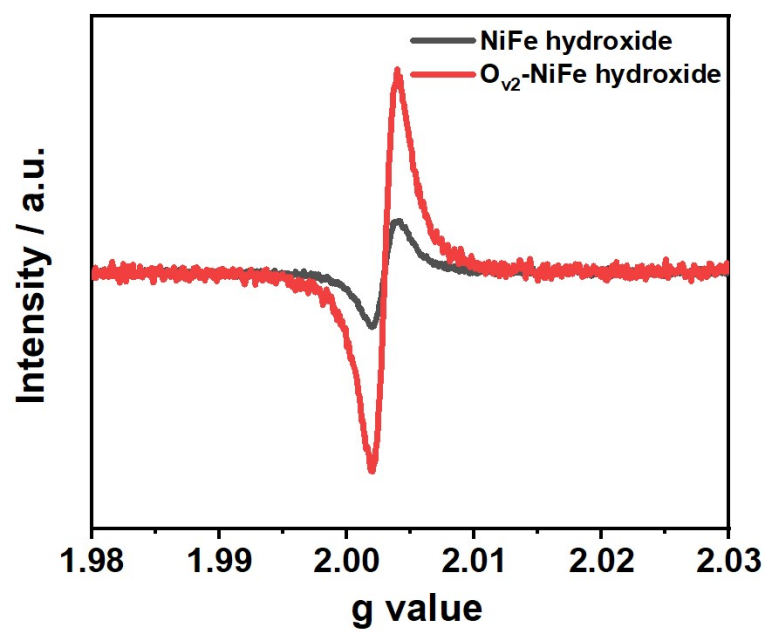
Fig. S8. The g value for O_v-NiFe hydroxide and NiFe hydroxide.
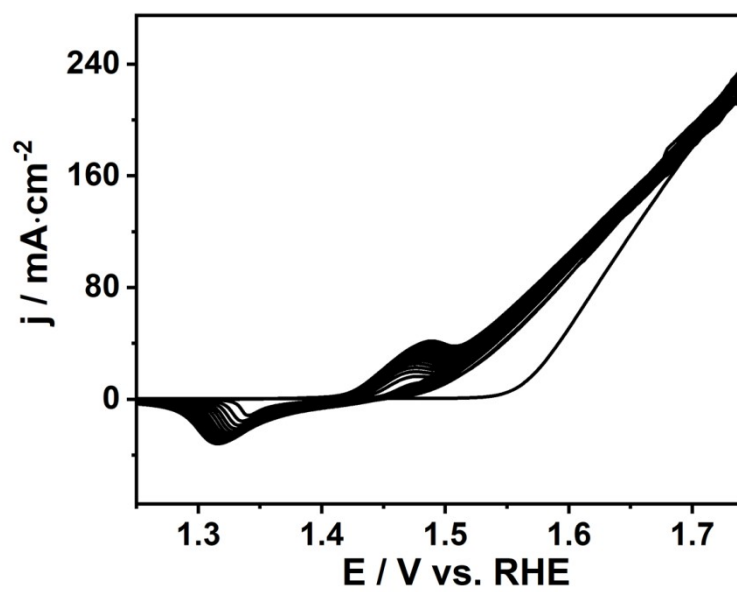
Fig. S9. Voltammetric activation process of O_{v2}-NiFe hydroxide for OER.
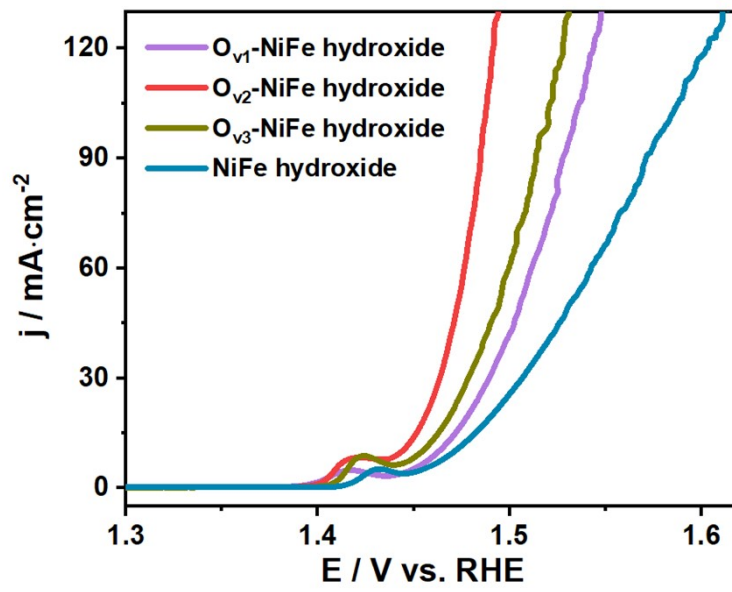
Fig. S10. The LSV polarization curves of O_v-NiFe hydroxide with different O_v content in the O_2 saturated 1.0 KOH with 95% iR corrected.
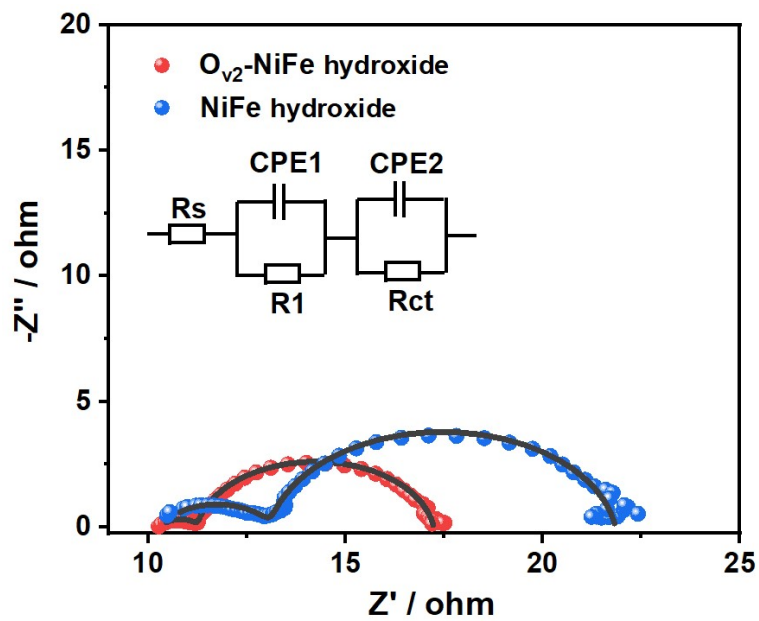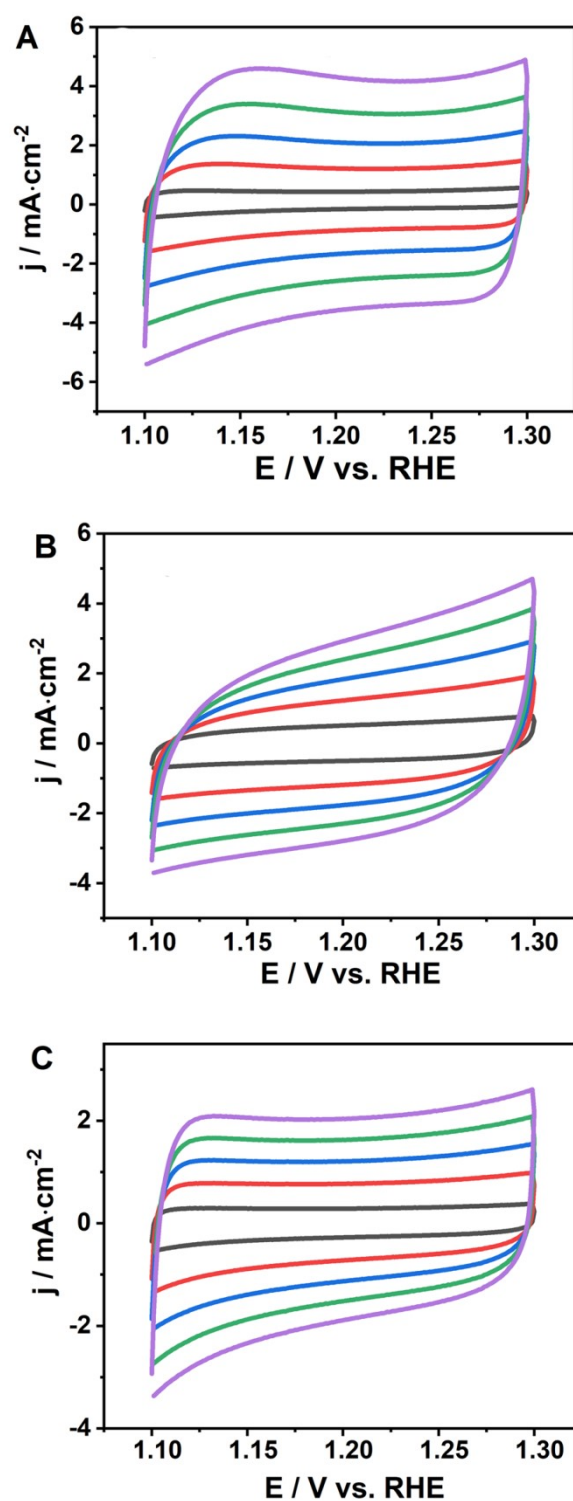
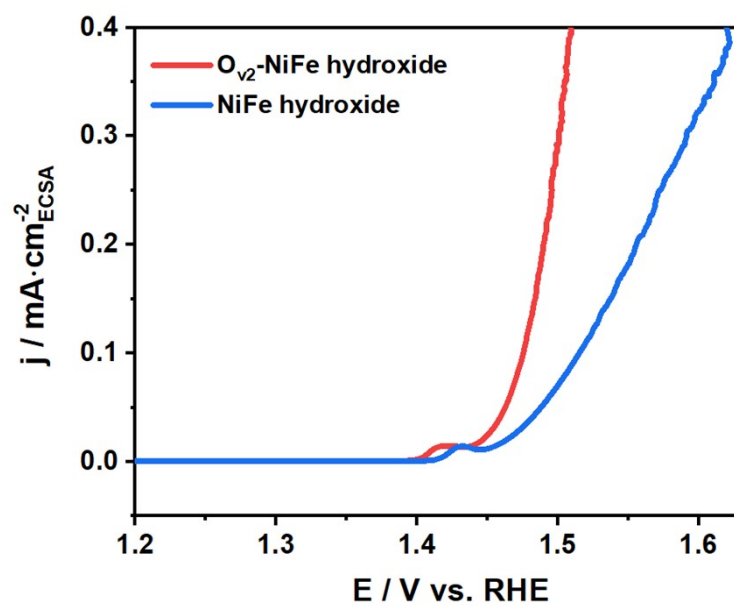**Fig. S11**. Nyquist plots of O_{v2}-NiFe hydroxide and NiFe hydroxide at the overpotential of 245 mV.
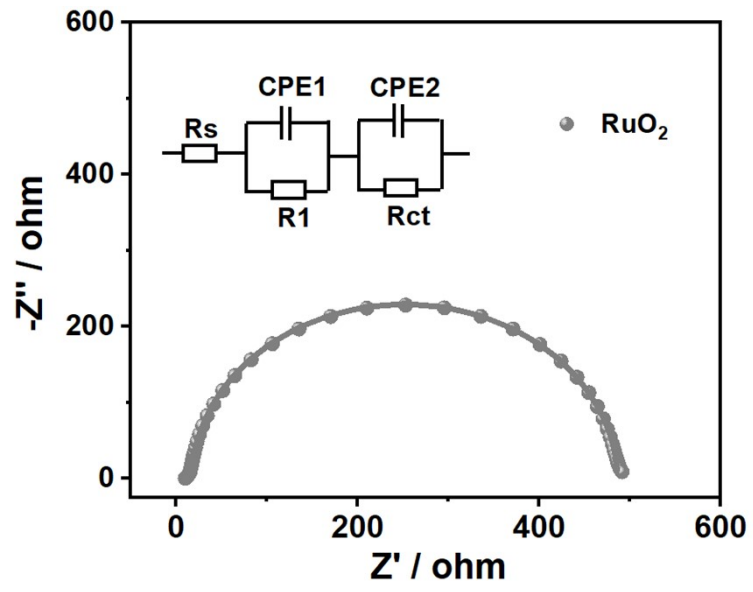
**Fig. S12.** Nyquist plots of RuO_2 at the overpotential of 245 mV.

Fig. S13. The cyclic voltammetry (**A**) O_{v2}-NiFe hydroxide, (**B**) NiFe hydroxide, (**C**) RuO_2 in O_2-saturated 1.0 M KOH at different scan rates at 20, 60, 100, 140, and 180 $mV \cdot s^{-1}$.

Fig. S14. The specific activity of Ov_2-NiFe hydroxide and NiFe hydroxide at the applied potential.
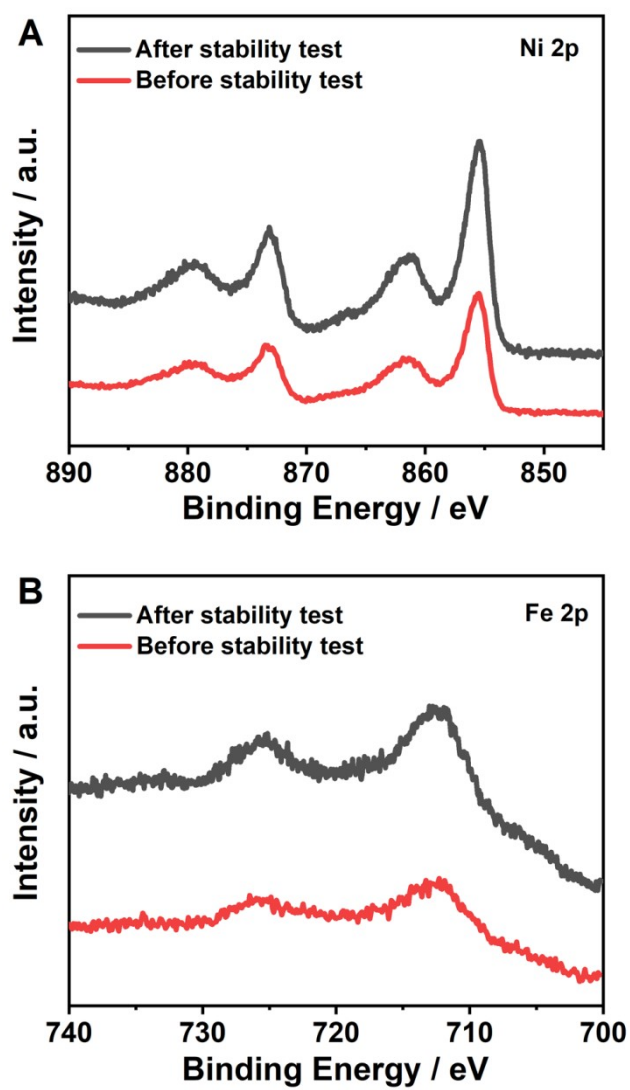
Fig. S15. The Ni 2p and Fe 2p after stability test for O_{v2}-NiFe hydroxide.
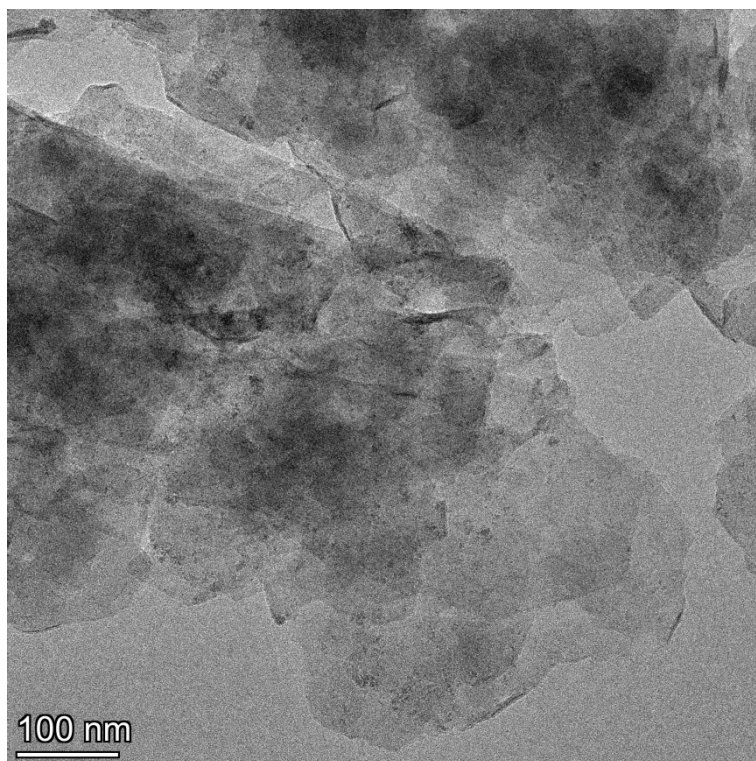
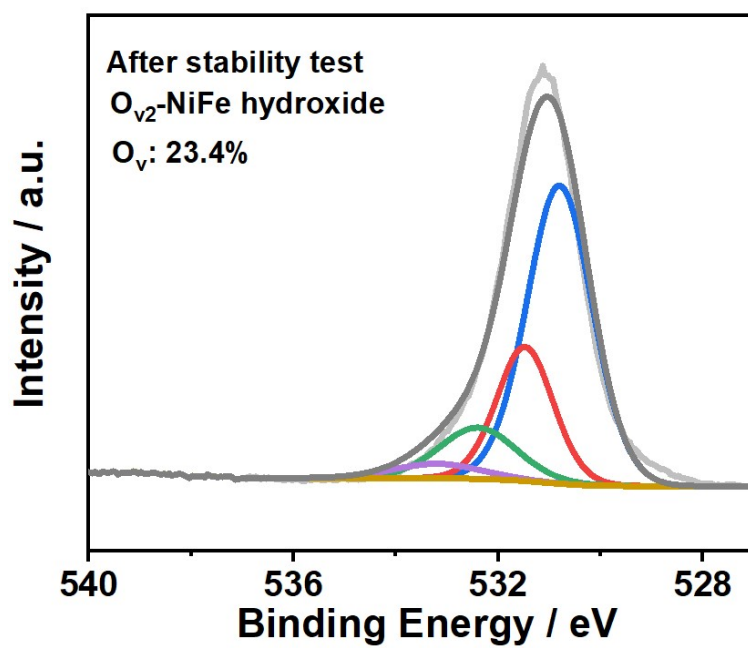**Fig. S16**. The TEM image of O_{v2}-NiFe hydroxide after stability test.
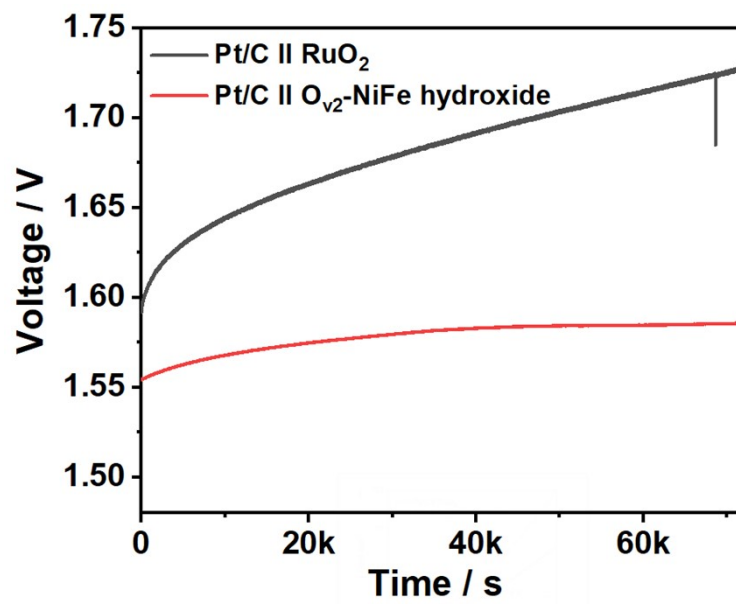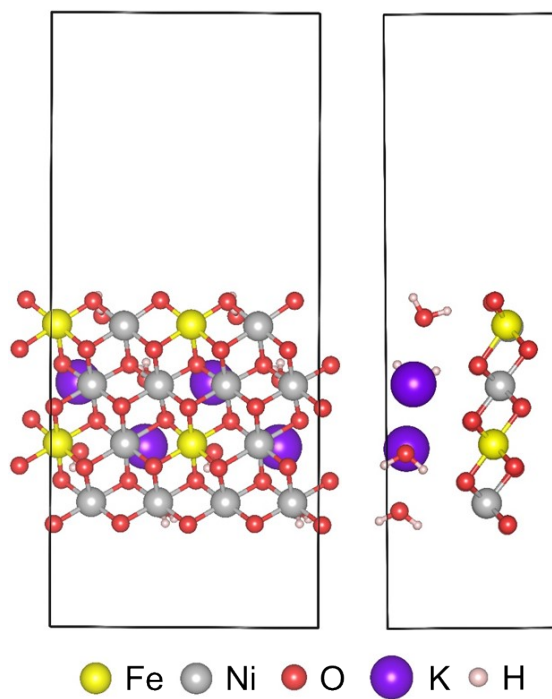
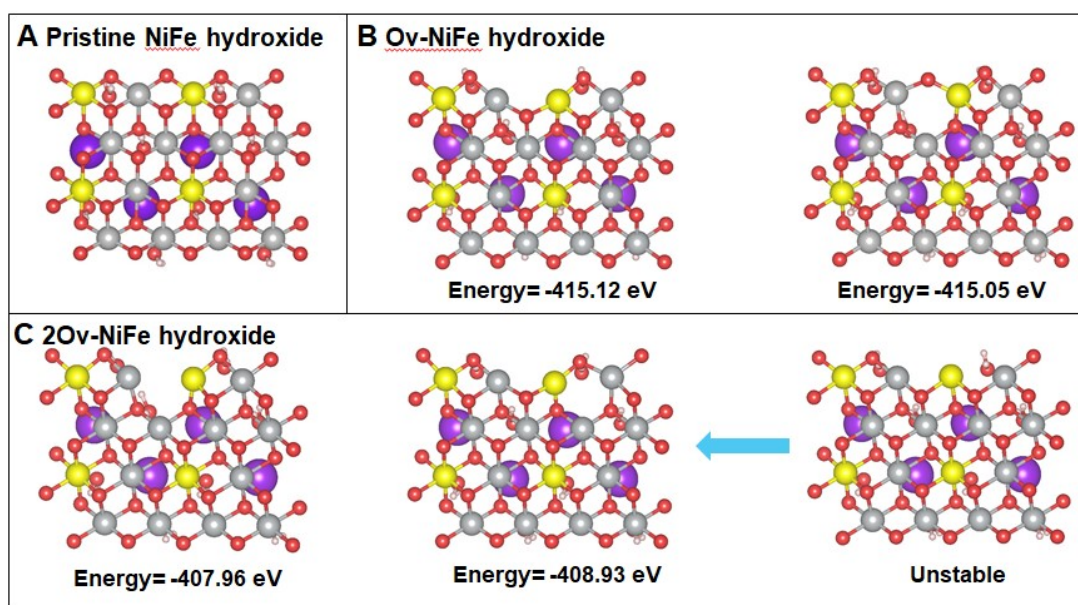**Fig. S17**. O 1s after stability test for O_{v2}-NiFe hydroxide.

Fig. S18. The stability of Pt/C II RuO$_2$ and Pt/C II O$_{v2}$-NiFe hydroxide at 10 mA·cm^{-2}.
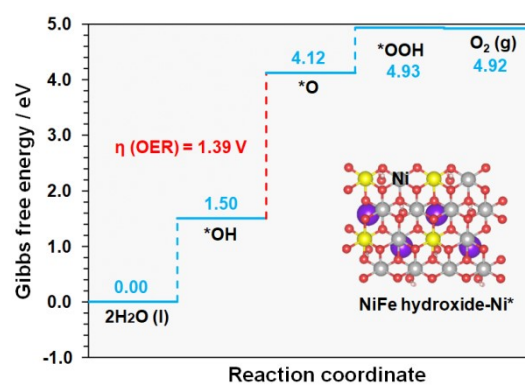
Fig. S19. The side views configuration of pristine NiFe hydroxide, with chemical formula $K_{1/3}(H_2O)_{2/3}(Ni,Fe)O_2$ [yellow for Fe, gray for Ni, red for O, purple for K, and white for H].
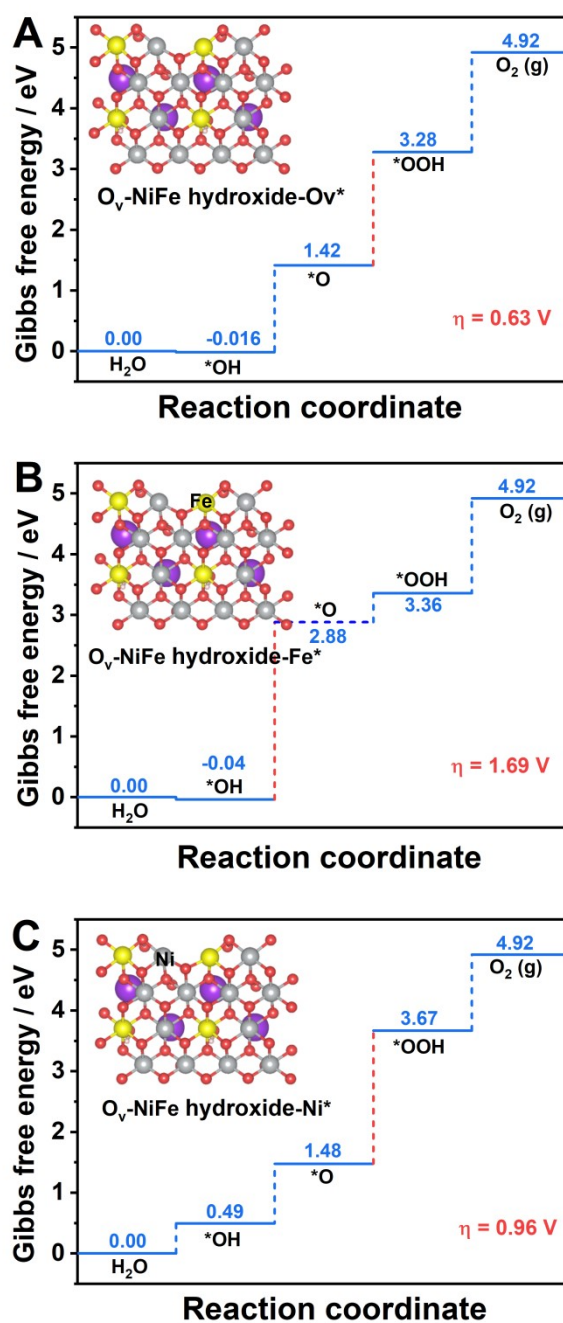
Fig. S20. Total energy and corresponding configuration of (**A**) pristine NiFe hydroxide, (**B**) O_v-NiFe hydroxide and (**C**) $2O_v$-NiFe hydroxide. The lowest energy represents the most stable structure.

Fig. S21. Free energy diagram on NiFe hydroxide-Ni* at zero potential (U=0) for OER

Fig. S22. OER free energy diagram for (**A**) O_v, (**B**) Fe and (**C**) Ni sites on O_v-NiFe hydroxide at zero potential (U = 0), red dotted line represents the potential limiting step (PLS).
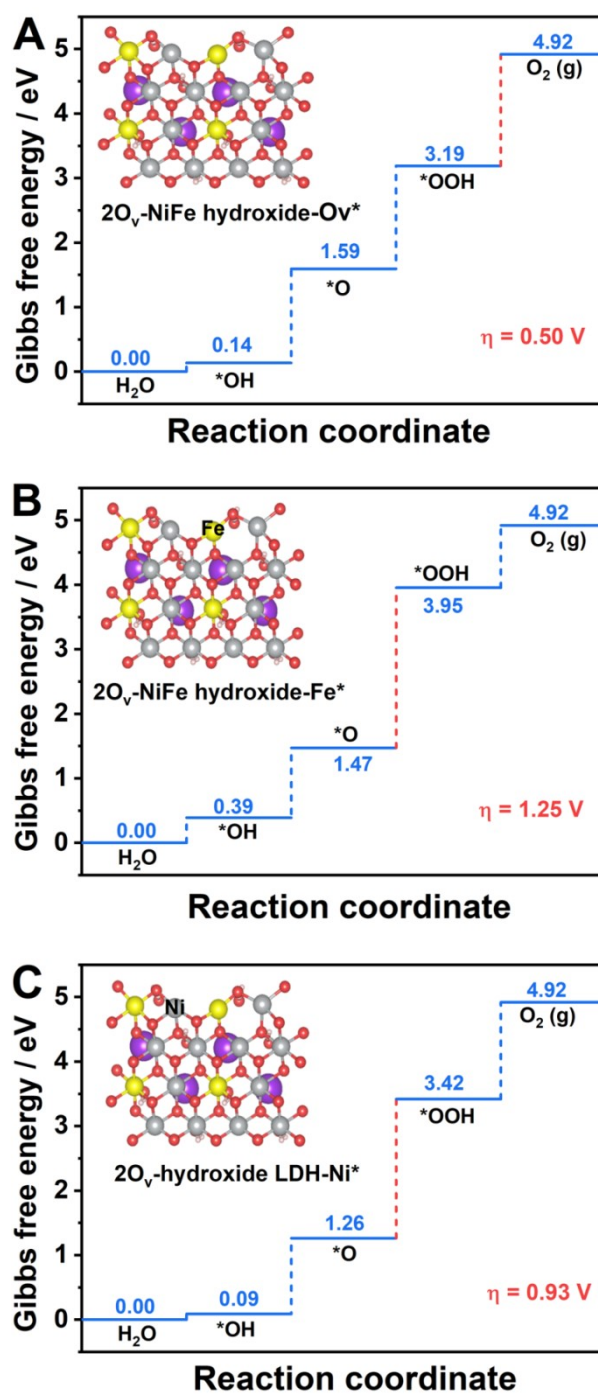
Fig. S23. OER free energy diagram for (**A**) O_v, (**B**) Fe and (**C**) Ni sites on $2O_v$-NiFe hydroxide at zero potential (U = 0), red dotted line represents the potential limiting step (PLS).
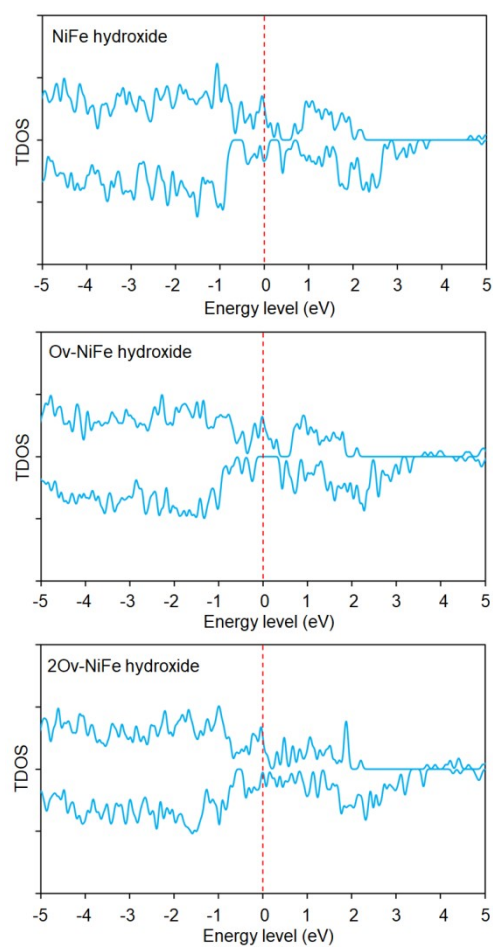
Fig. S24. The total density of states (TDOS) analysis of NiFe hydroxide, O_v-NiFe hydroxide and $2O_v$-NiFe hydroxide.
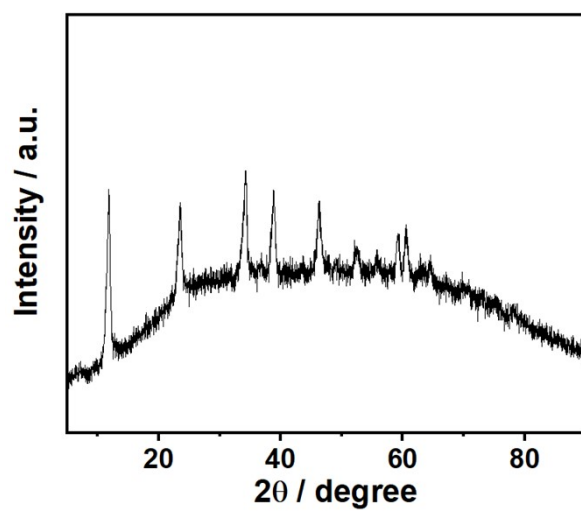
Fig. S25. XRD patterns of O$_v$-CoFe hydroxide.
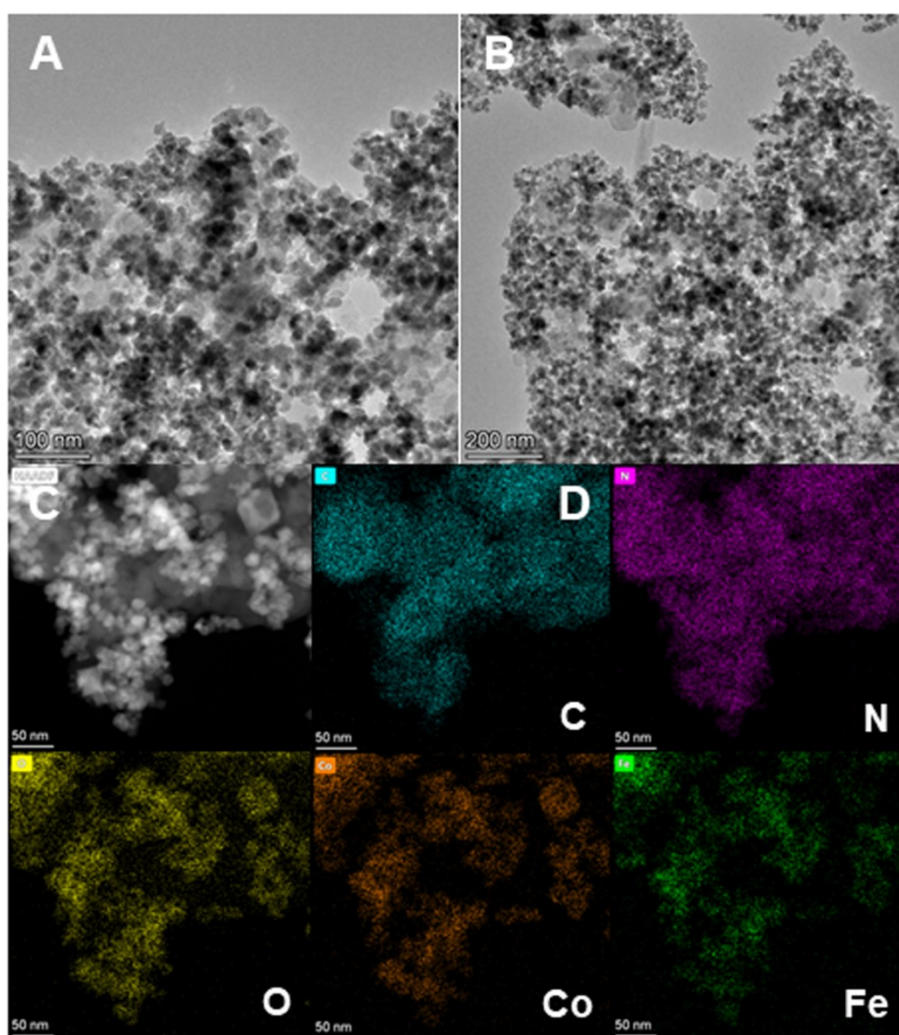
Fig. S26. TEM image of (A) O_v-CoFe hydroxide and (B) CoFe hydroxide; (C) HADDF-STEM image and (D) corresponding EDS mapping of O_v-CoFe hydroxide.

Fig. S27. Full scan XPS spectra of O_v-CoFe hydroxide and CoFe hydroxide.
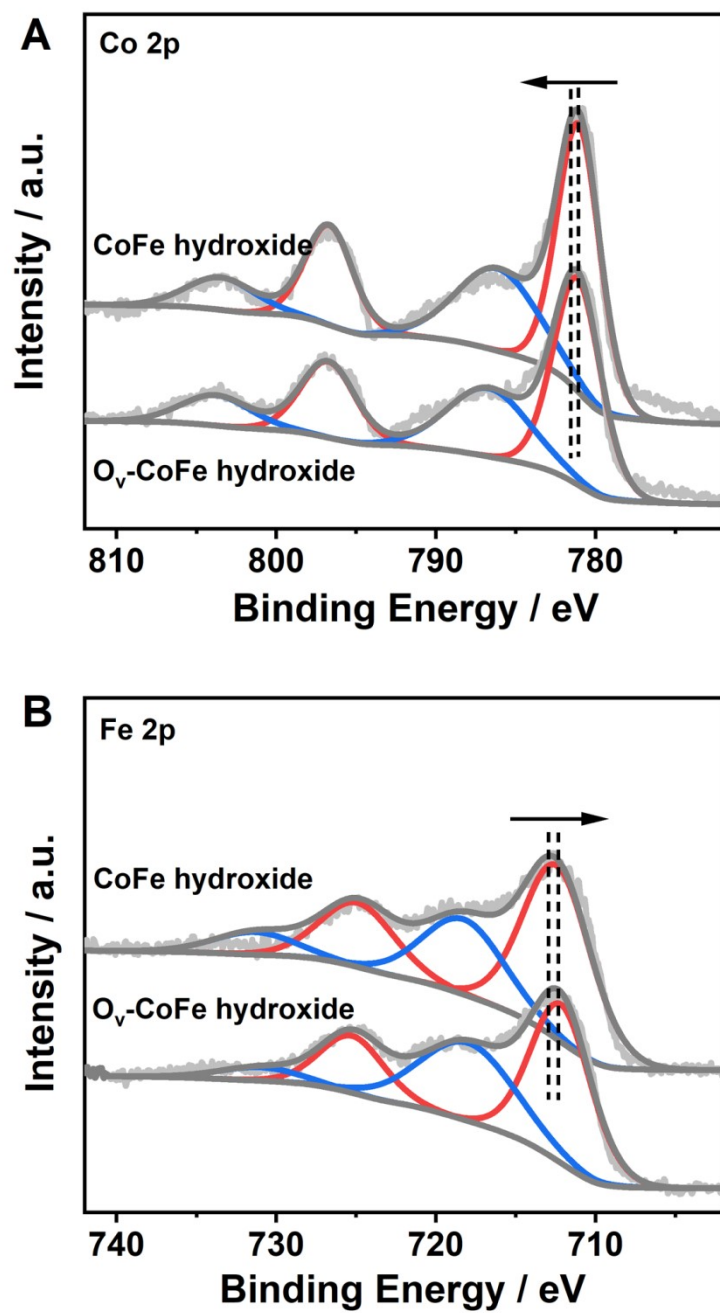
Fig. S28. XPS spectra of O_v-CoFe hydroxide and CoFe hydroxide.
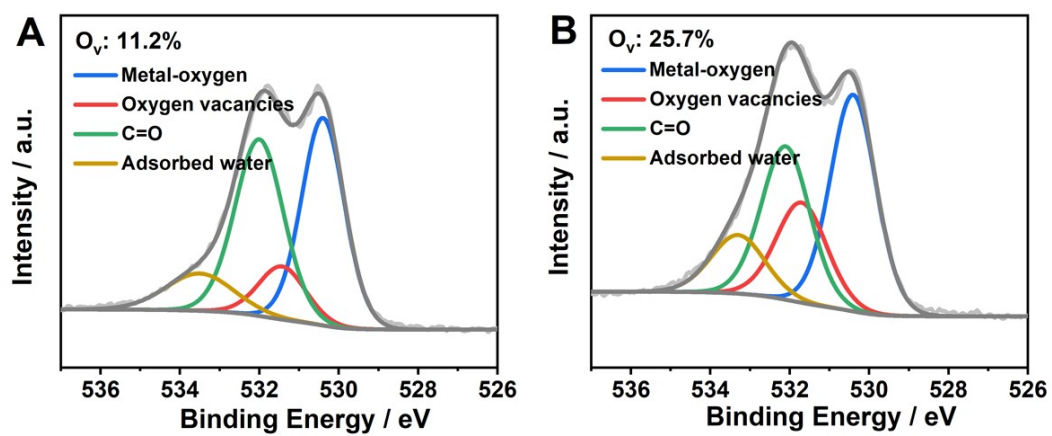
Fig. S29. O 1s of CoFe hydroxide and O_v-CoFe hydroxide.

Fig. S30. The EPR spectra of O_v-CoFe hydroxide and CoFe hydroxide.

Fig. S31. The g value of O_v-CoFe hydroxide and CoFe hydroxide.

Fig. S32. XRD patterns of O_v-CoNi hydroxide.
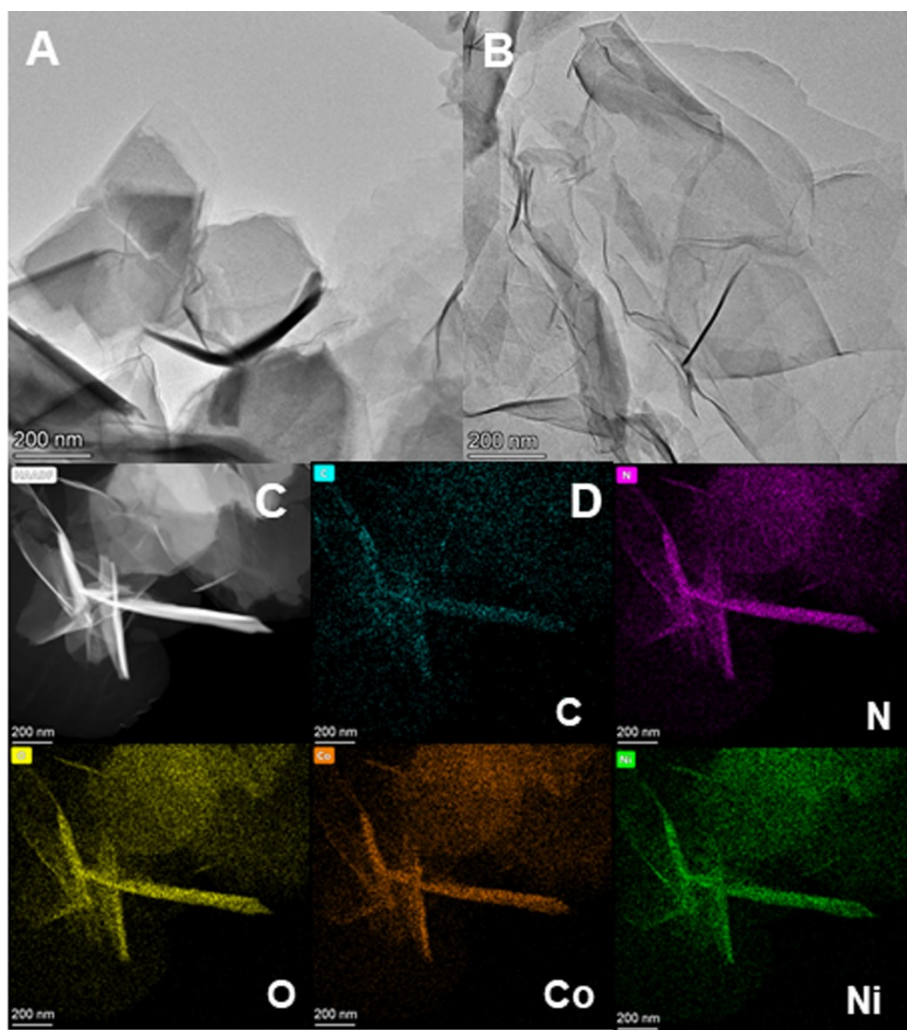
Fig. S33. TEM image of (**A**) O_v-CoNi hydroxide and (**B**) CoNi hydroxide; (**C**) HADDF-STEM image and (**D**) corresponding EDS mapping of O_v-CoNi hydroxide.
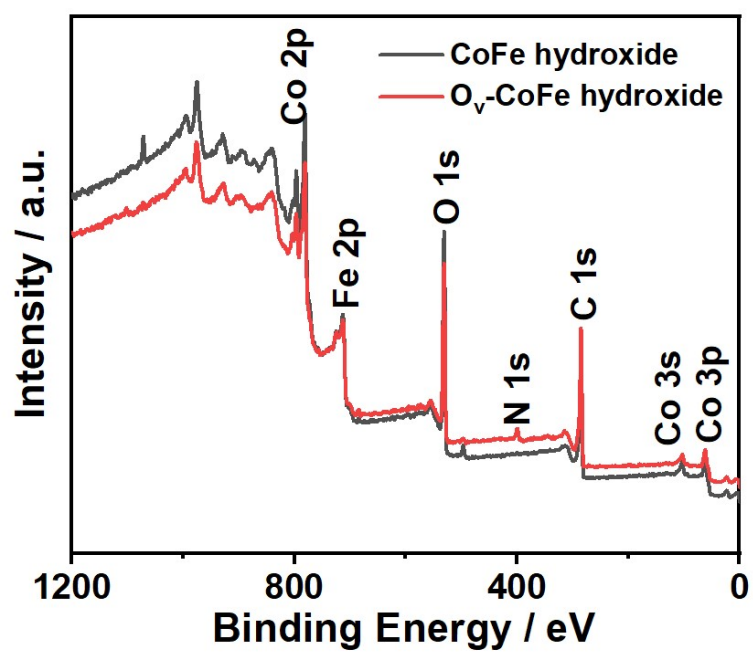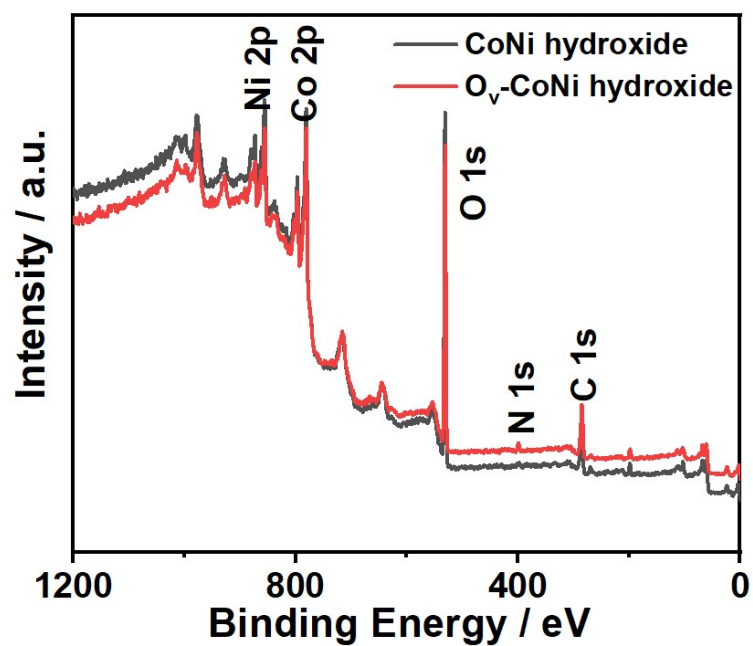
Fig. S34. Full scan XPS spectra of O_v-CoNi hydroxide and CoNi hydroxide.

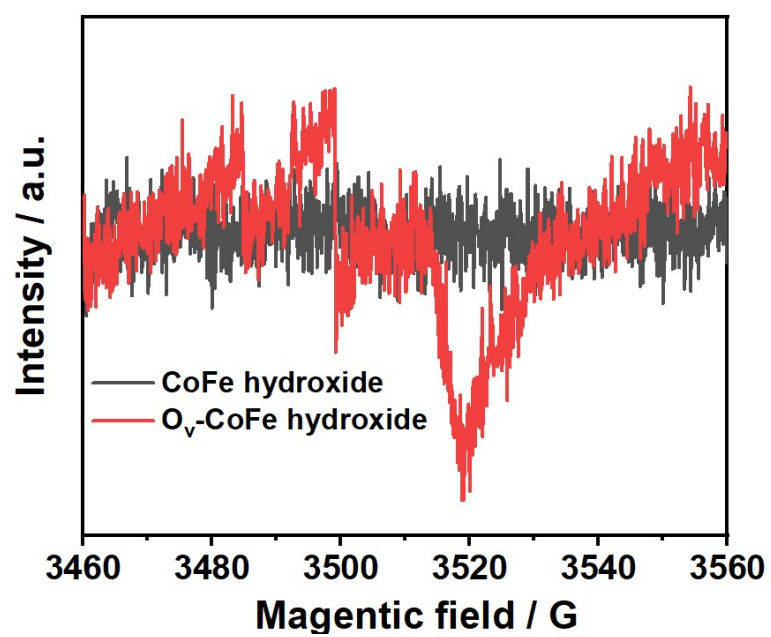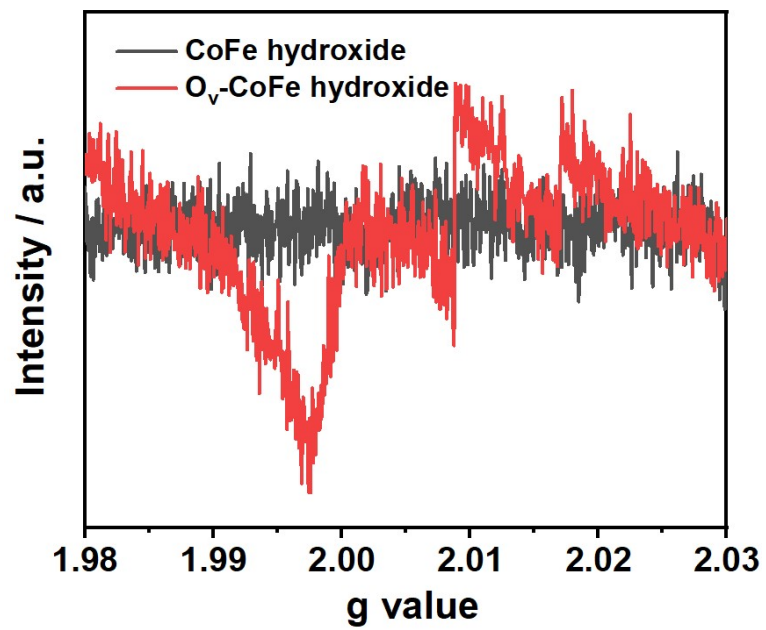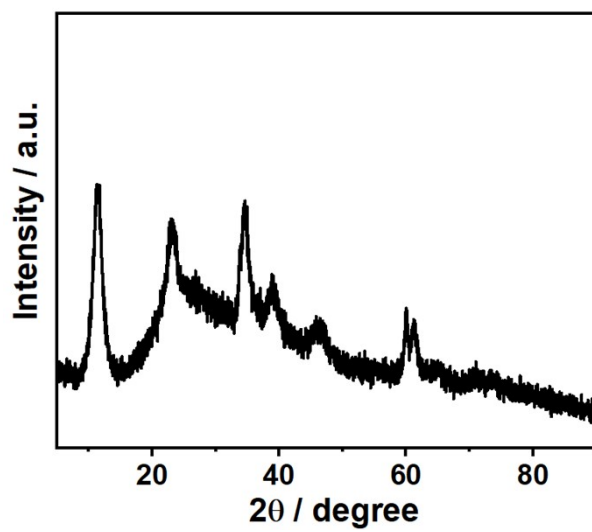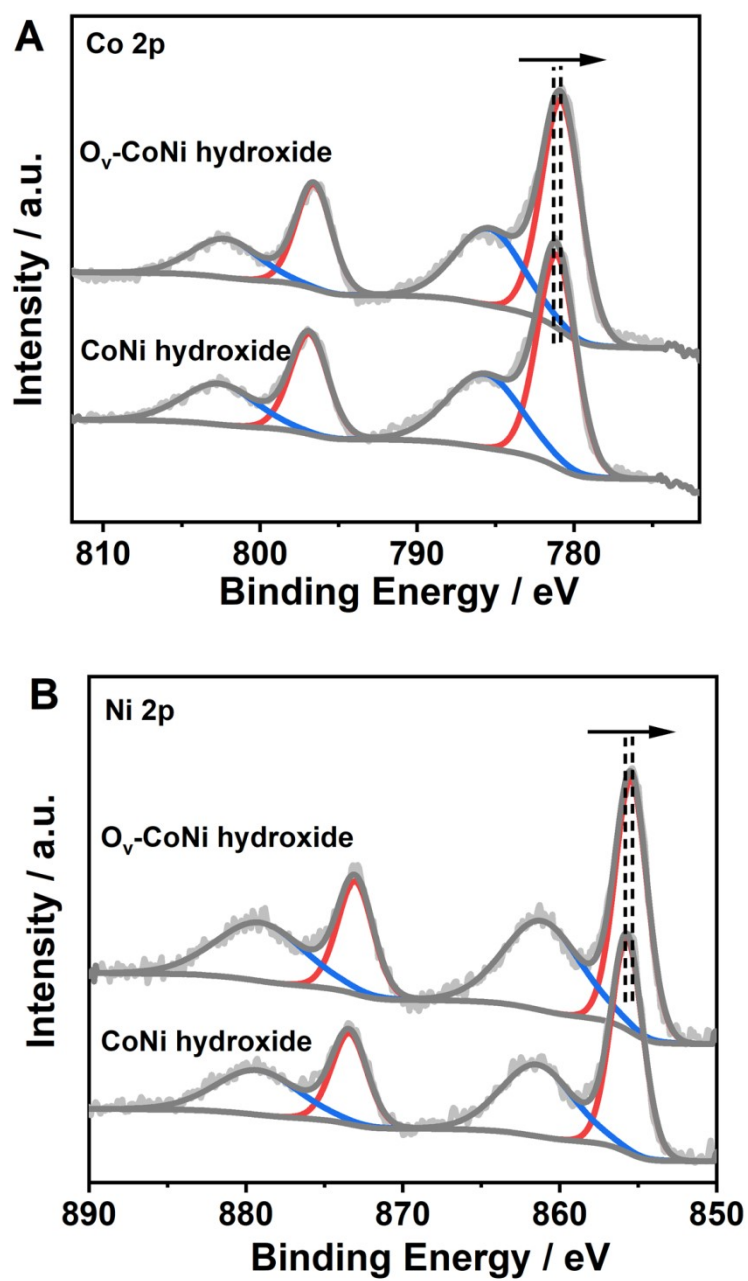**Fig. S35.** XPS spectra of O_v-CoNi hydroxide and CoNi hydroxide
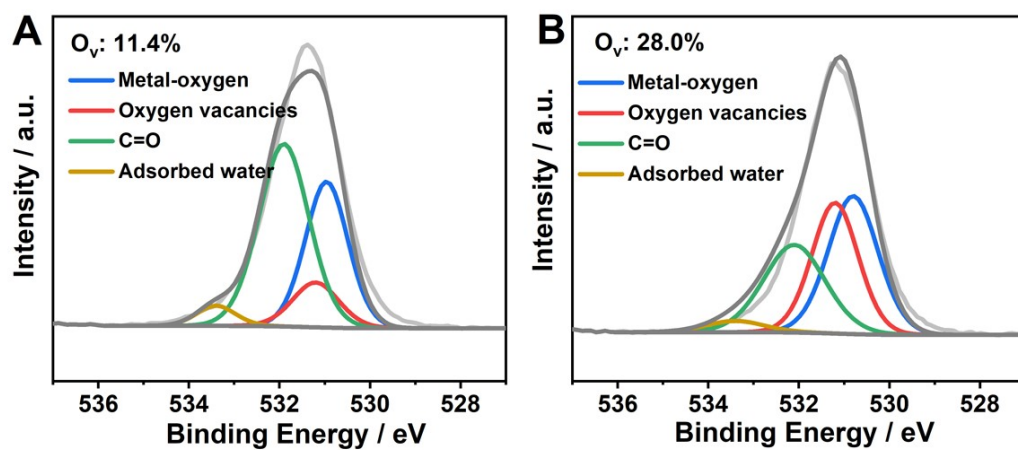
Fig. S36. O 1s of CoNi hydroxide and O$_v$-CoNi hydroxide.
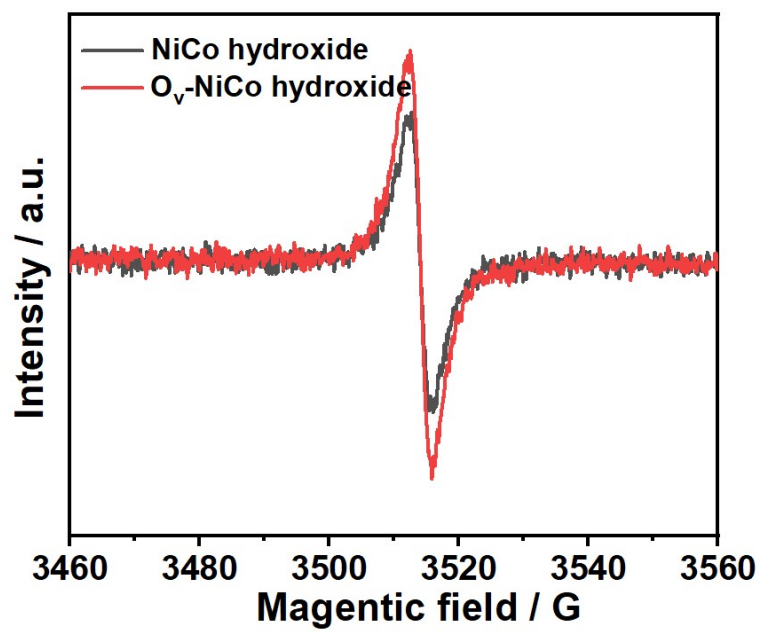
Fig. S37. The EPR spectra of O$_v$-CoNi hydroxide and CoNi hydroxide
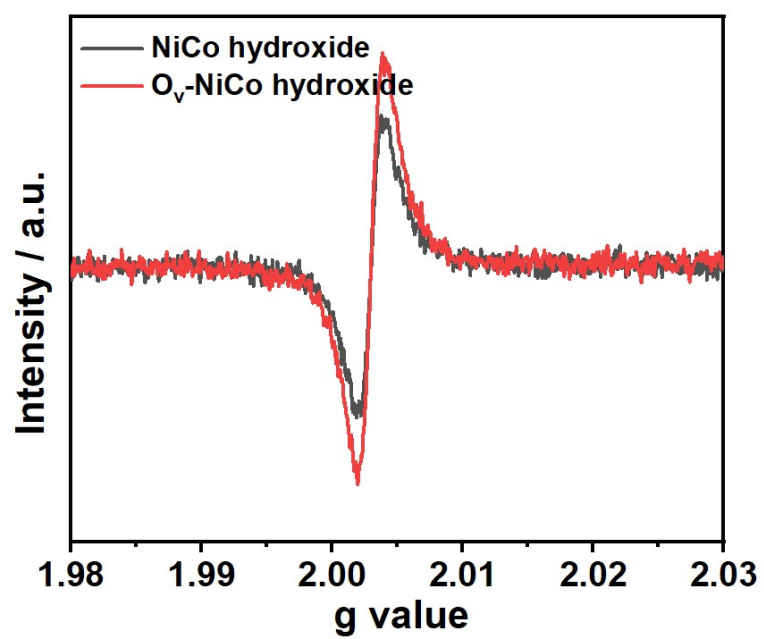
Fig. S38. The g values of O_v-CoNi hydroxide and CoNi hydroxide.
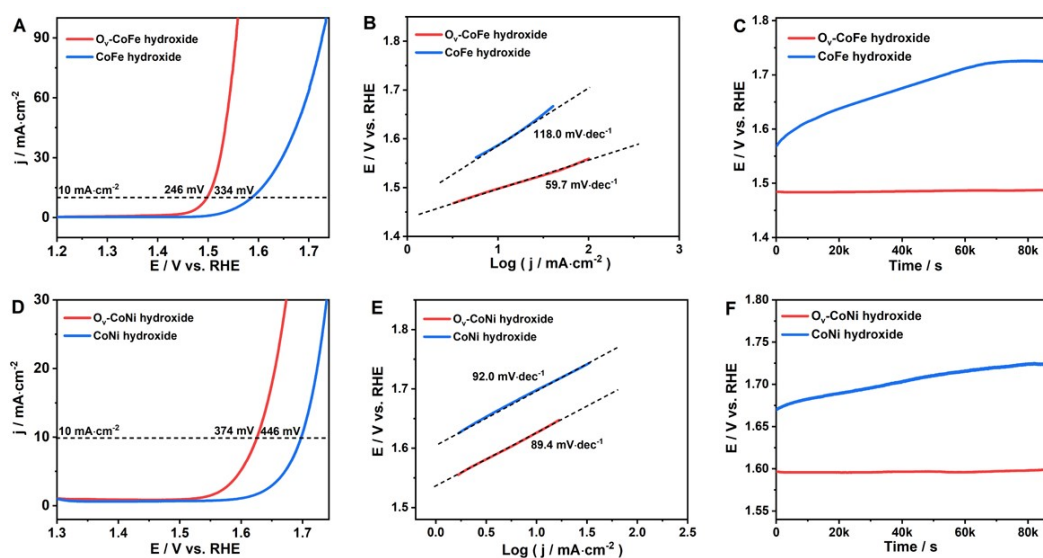
Fig. S39. **OER activity of O$_v$-CoFe hydroxide and O$_v$-CoNi hydroxide.** (**A**) The LSV curves of O$_v$-CoFe hydroxide and CoFe hydroxide in the O$_2$ saturated 1.0 KOH, (**B**) LSV curves of O$_v$-CoFe hydroxide and CoFe hydroxide in the O$_2$ saturated 1.0 KOH, (**C**) Potentiostatic curves for O$_v$-CoFe hydroxide and CoFe hydroxide at 10 mA·cm^{-2}. (**D**) The LSV curves of O$_v$-CoNi hydroxide and CoNi hydroxide in the O$_2$ saturated 1.0 KOH, (**E**) LSV curves of O$_v$-CoNi hydroxide and CoNi hydroxide in the O$_2$ saturated 1.0 KOH, (**F**) Potentiostatic curves for O$_v$-CoNi hydroxide and CoNi hydroxide at 10 mA·cm^{-2}.

Supplementary Note 1: Structure characterization and electrocatalytic activity

To evaluate the generality of the role of CN on transition metal layered double hydroxide, O_v-CoFe hydroxide and O_v-CoNi hydroxide are fabricated with CN and as OER electrocatalysts. **Fig. S25** and **S26** reveal that the sheet-like O_v-CoFe hydroxide and CoFe hydroxide are successfully achieved via the hydrothermal approach. The full scan XPS spectra exhibit that constituent elements are mainly C, O, Co and Fe elements for CoFe hydroxide. Furthermore, an obvious N signal can be observed for O_v-CoFe hydroxide (**Fig. S27**). Compared with CoFe hydroxide, the peak of Co 2p of O_v-CoFe hydroxide moves to positive binding energy, and Fe 2p XPS spectra O_v-CoFe hydroxide exhibits the negative shift (**Fig. S28**). Meanwhile, Co 2p XPS spectra of O_v-CoFe hydroxide can be fitting with Co 2p3/2 (781.2 eV) and Co 2p1/2 (796.7 eV), and other two peaks are assigned to the Co sat [S8]. Additionally, the Fe^{3+} and Fe sat. signals can be clearly observed from high resolution Fe 2p XPS spectra [S9]. O 1s XPS spectra confirm that CN is beneficial to producing the oxygen vacancies. Specially, the oxygen vacancies in O_v-CoFe hydroxide are calculated to be 25.7 %, the value is higher than that of CoFe hydroxide (**Fig. S29**). The EPR spectra confirm that the peak density of O_v-CoFe hydroxide is stronger than that of CoFe hydroxide (**Fig. S30** and **S31**). Furthermore, the structure and morphology characterization exhibit that sheet-like O_v-CoNi hydroxide and CoNi hydroxide are successfully achieved (**Fig. S32** and **S33**). Compared with CoNi hydroxide, an obvious N singal can be observed for O_v-CoNi hydroxide, suggesting the introduction of CN in O_v-CoNi hydroxide (**Fig. S34**). **Fig. S35** suggests that Co 2p and Ni 2p of O_v-CoNi hydroxide shift to negative binding energy against those of CoNi hydroxide. The high resolution Co 2p XPS spectra shows that the peaks loaded at the 780.8 eV and 785.4 eV correspond to Co $2p_{3/2}$ and Co $2p_{1/2}$ of Co^{2+}, respectively. The other two peaks are attributed to Co satellite. For Ni 2p spectra, the peaks at about 855.4 eV and 861.1 eV are attributed to Ni(II) $2p_{3/2}$ and Ni(II) $2p_{1/2}$ and another peak reflect the Ni satellite [S10]. From O 1s XPS spectra, oxygen vacancies in CoNi hydroxide and O_v-CoNi hydroxide are calculated to be 11.4% and 28.0%, respectively (**Fig. S36**). EPR

measurements demonstrate that the density of oxygen vacancies of O_v-CoNi hydroxide is higher than that of CoNi hydroxide (**Fig. S37** and **S38**).

The electrochemical experiments exhibit that O_v-CoFe hydroxide offers the excellent OER performances with low overpotential (268 mV) to drive 10 mA·cm^{-2} and small values of Tafel slope (59.7 mV·dec^{-1}), which is much superior to CoFe hydroxide (356 mV at 10 mA·cm^{-2}, Tafel slope of 118 mV·dec^{-1}). Furthermore, O_v-CoFe hydroxide also exhibit good stability compared with CoFe hydroxide by chronoamperometric technology after 24 h test at the current density of 10 mA·cm^{-2} (**Fig. S39A-C**). Notably, O_v-CoNi hydroxide represent the overpotential of 396 mV to derive 10 mA·cm^{-2} and low Tafel slope of 89.4 mV·dec^{-1}, which is superior to that of CoNi hydroxide (468 mV at 10 mA·cm^{-2}, Tafel slope of 92.0 mV·dec^{-1}). Importantly, the O_v-CoNi hydroxide also exhibits the remarkable stability with respect to CoNi hydroxide. It can be concluded that the strategy of carbon nitride modulated oxygen vacancies is a general method to design highly efficient electrocatalyst based on transition metal layered double hydroxide (**Fig. S39D-F**).

Table S1 The metal content in the achieved composite.

Composite	Ni content (wt%)	Fe content (wt%)	Co content (wt%)
NiFe hydroxide	21.8	7.5	-
O_{v1}-NiFe hydroxide	21.6	7.4	-
O_{v2}-NiFe hydroxide	30.9	10.5	-
O_{v3}-NiFe hydroxide	29.6	9.9	-
CoFe hydroxide	-	15.2	32.8
O_v-CoFe hydroxide	-	17.9	37.1
CoNi hydroxide	18.4	-	28.5
O_v-CoNi hydroxide	18.1	-	29.1

Table S2 Comparison of the OER performance of as-achieved elecrocatalysts with the most recently reported OER catalysts at 10 mA·cm^{-2}.

Catalyst	electrolyte	The overpotential at 10 mA·cm^{-2} (mV)	Tafel slope (mV·dec^{-1})	Reference
O$_{v2}$-NiFe hydroxide	**1.0 M KOH**	**214**	**43.0**	**This work**
O$_v$-CoFe hydroxide	**1.0 M KOH**	**268**	**59.7**	**This work**
O$_v$-CoNi hydroxide	**1.0 M KOH**	**396**	**89.4**	**This work**
ANC Fe$_1$Ni$_2$	1.0 M KOH	266	39	J. Energy Chem., 2022, 71, 167–173
CoFe LDH/rGO	0.1 M KOH	396	43	Adv. Mater. Interfaces, 2016, 3, 1500782
NP Au/Cr–NiFe	0.1 M KOH	323	33	J. Mater. Chem. A, 2019, 7, 9690 - 9697
NiCoFe-LDH HP	1.0 M KOH	276	56	J. Energy Chem., 2020, 43, 104 - 107
E-CoFe LDHs	1.0 M KOH	300	41	Chem. Commun., 2017, 53, 11778–11781
Exfoliated NiCo NS	1.0 M KOH	334	41	Nat. Commun., 2014, 5, 4477
CoNi LDH/CoO	1.0 M KOH	300	123	Nano Res., 2016, 9, 713 – 725
Co$_3$O$_4$/CeO$_2$ NHs	1.0 M KOH	270	60	Adv. Mater. 2019, 31, 1900062
Mn-NiFe LDH/rGO	1.0 M KOH	256	40	Sci. China. Mater., 2021, 64, 2729–2738
NiFe LDH HMS	1.0 M KOH	239	53	ACS Appl. Mater. Interfaces, 2016, 8, 33697–33703，
v-NiFe LDH	1.0 M KOH	210	34.8	Nano Energy, 2021, 81, 105606
NiFe LDHs–VNi	1.0 M KOH	229	62.9	Small, 2018, 14, 1800136.
3D NiFe- LDH HMS	1.0 M KOH	290	51	J. Energy Chem., 2019, 33, 130–137
Ni–Fe LDH nanocages	1.0 M KOH	246@20	71	Adv. Mater., 2020, 32, 1906432
Monolayer NiFe LDH	1.0 M KOH	230	47	Adv. Energy Mater., 2019, 9, 1900881
ZnNi LDH/N-rGO	1.0 M KOH	290	44	Nanoscale, 2017, 9, 12590 - 12600
Ni$_{1.5}$Sn@triMPO$_{4-R}$/CC	1.0 M KOH	240	45.2	Angew. Chem. Int. Ed., 2021, 60, 3773-3780
Co$_5$Mn LDH/MWCNT	1.0 M KOH	300	73.6	ACS Appl. Mater. Interfaces, 2016, 8, 14527 - 14534.
TiN@Co$_{5.47}$N/Ti	1.0 M KOH	211	42.5	Adv. Funct. Mater., 2021, 31, 2008511
5.0% Ce-NiFe-LDH/CNT	1.0 M KOH	227	33	ACS Appl. Mater. Interfaces, 2018, 10, 6336 - 6345
Ni-MOF/LDH/NF	1.0 M KOH	220	36	Appl. Catal. B: Environ., 2021, 286, 119906.
(Ni$_x$Fe$_y$Co$_{6-x-y}$)Mo$_6$C/NF	1.0 M KOH	212	55.1	Appl. Catal. B: Environ., 2021, 290, 120049.

References

S1 G. Kresse, *Phys. Rev. B*, 1996, **54**, 11169e86.

S2 G. K. J. Furthmu¨ller, *Phys. Rev. B*, 1999, **54**, 11169-86.

S3 J.-J. Tang and B. Liu, *J. Phys. Chem. C*, 2016, **120**, 6642-50.

S4 M. Capdevila-Cortada, Z. Łodziana and N. López, *ACS Catal.*, 2016, **6**, 8370-9.

S5 Y. Dong, P. Zhang, Y. Kou, Z. Yang, Y. Li ,X. Sun, *Catal. Lett.*, 2015, **145**, 1541-8.

S6 J. A. Stefan Grimme, S. Ehrlich and H. Krieg, *J. Chem. Phys.*, 2010, **132**, 154104.

S7 K. Momma and F. Izumi, *J. Appl. Crystallogr.*, 2008, **41**, 653-8.

S8 H. Wang, Y. Yuan, J. L. Gu, Z. C. Jia, Z. S. Lu, Z. Y. Bai, L. Yang and X. L. Yang, *J. Power Sources*, 2020, **467**, 228354.

S9 T. Yamashita and P. Hayes, *Appl. Surf. Sci.*, 2008, **254**, 2441.

S10 F. Song and X. L. Hu, *Nat. Commun.*, 2014, **5**, 4477.